Attitude Reconstruction of a Spacecraft from Temperature Measurements in Solar Eclipse

Analysis and Observer Design for a Not Globally Observable Non-Linear System

Tobias Posielek, Johann Reger

This article proposes a method that uses only a single temperature measurement and angular velocity measurements to estimate the attitude of a spacecraft under the influence of solely infrared irradiation. The system governing the dynamics is highly non-linear with its attitude being defined in the quaternion space. The resulting observability mapping is used to transform the system into a canonical observability form. However, this mapping is not bijective, and a method to find the arising local inverses is proposed. The reconstruction algorithm itself is divided into two separate parts and uses the canonical form. The first part carries out the dynamic estimation of the temperature and its derivatives. The second part uses these derivatives to estimate the attitude by solving a system of non-linear equations. The proposed algorithm achieves the desired results under the assumption that a suitable initial guess of the attitude is available. Numerical simulations show the validity of the algorithm and illustrate errors induced by measurement noise.

Tobias Posielek, Johann Reger: Attitude Reconstruction of a Spacecraft from Temperature Measurements in Solar Eclipse Analysis and Observer Design for a Not Globally Observable Non-Linear System, IEEE Transactions on Control Systems Technology 2022, DOI: 10.1109/TCST.2022.3187916

Attitude Reconstruction of a Spacecraft from Temperature Measurements in Solar Eclipse

Analysis and Observer Design for a not Globally Observable Non-Linear System

Tobias Posielek and Johann Reger

***Abstract*— This paper proposes a method that uses only a single temperature measurement and angular velocity measurements to estimate the attitude of a spacecraft under the influence of solely infrared irradiation. The system governing the dynamics is highly non-linear with its attitude being defined in the quaternion space. The resulting observability mapping is used to transform the system into canonical observability form. However, this mapping is not bijective and a method to find the arising local inverses is proposed. The reconstruction algorithm itself is divided into two separate parts and uses the canonical form. The first part carries out the dynamic estimation of the temperature and its derivatives. The second part uses these derivatives to estimate the attitude by solving a system of non-linear equations. The proposed algorithm achieves the desired results under the assumption that a suitable initial guess of the attitude is available. Numerical simulations show the validity of the algorithm and illustrate errors induced by measurement noise.**

I. Introduction

Attitude determination and control is a vital part in every space mission design. Different missions demand different attitudes with different precisions. The attitude is usually obtained using a combination of multiple sensors such as star trackers, Sun sensors, Earth sensors, gyroscopes and GPS, see e.g. [1] and [2]. Their signals are fused in order to obtain an optimal attitude estimation [3]. Due to the importance of the subject, additional ways are always investigated to obtain new options to estimate the attitude in a more cost effective and robust way. Currently, the capabilities of temperature sensors for attitude and position estimation is a vivid subject of research. The common assumption is that satellite surfaces are equipped with temperature sensors that are thermally isolated from inner heat flows and the heat flows from other surfaces which makes their temperature evolution governed only by the environmental heat flows. Thus, the temperature dynamics are defined by the superposition of solar, albedo, infrared and deep space irradiation, the first three depending on the attitude and the position of Earth and Sun. A model based on this assumption is validated in [4] using commercial thermal analysis tools for a typical low Earth orbit. The temperatures resulting from the model follow closely the results of the thermal analysis tools with maximal deviations of about 5 degrees Celsius. The same model is validated by [5], who have constructed and tested a cubic laboratory satellite in a vacuum chamber equipped with a Sun simulator. They have found that the proposed models gives satisfying results for the proposed experimental setup with three isolated copper surfaces. The resulting temperature data can be used for orbit determination, estimating the position and velocity of the spacecraft as shown in [6]. Here, it is exploited that two of the main irradiations acting are emitted by the Earth, namely the albedo and infrared irradiation. The governing temperature dynamics are non-linear in position, temperature as well as attitude leading to the analysis of a non-linear system and the usage of an unscented Kalman Filter. In the follow up work [7], the focus lies on the additional simultaneous estimation of the albedo factor. This factor is often assumed to be constant over the course of an orbit but actually varies with the local terrain as well as cloud coverage. In comparison to these works, it is also investigated if the attitude can be estimated from temperature measurements assuming the position of the spacecraft is known. In [8], the heat flux of multiple temperature sensors orthogonal to each other is estimated and cast into a static non-linear system of equations which contains the attitude represented in Euler angles. This system is then solved using the Levenberg-Marquardt algorithm in order to obtain the attitude. Due to the attitude space of dimension three, it can only be expected with a minimum of three measurements to obtain an attitude estimation in this framework. However, each sensor flux is influenced by the sum of solar, albedo and infrared irradiation. The individual irradiations cannot be estimated using only three sensors as multiple attitudes can lead to the same sensor flux. Thus, [8] proposes to add an additional sensor in opposing direction to one of the existing sensors to solve this uniqueness issue. The recent work [9] uses three heat flow measurements to acquire the attitude estimation based on an unscented and extended Kalman filter. While the unscented Kalman filter yields

This paper is submitted on October 11, 2021. The second author gratefully acknowledges the financial support from European Union Horizon 2020 research and innovation program, Marie Skłodowska-Curie grant agreement No. 824046.

T. Posielek is with the Institute of System Dynamics and Control, German Aerospace Center (DLR), Muenchner Str. 20, D-82234 Wessling, Germany (e-mail: tobias.posielek@dlr.de)

J. Reger is with the Control Engineering Group, Technische Universität Ilmenau, P.O. Box 10 05 65, D-98684, Ilmenau, Germany (e-mail: johann.reger@tu-ilmenau.de)

better results in accuracy, performance, robustness and stability based on Monte Carlo simulation, it also suffers under higher execution time. An experimental validation of the extended Kalman filter can also be found in [5] which has admitted an accuracy of 0.2°. Naturally, these errors are expected to be higher under non-laboratory conditions. In industry, Coarse Earth Sun Sensors [10] are employed to obtain a rough estimation of the attitude. They consist of six pairs of temperature sensors. Each pair has two sensors with different visual absorption and each pair is pointing into another direction. These twelve measurements are combined in order to estimate the attitude which can be used for example for a safe mode [11].

All the presented contributions use multiple temperature sensors. In contrast to these approaches, we are interested in how much information can be provided by a single temperature sensor. In this context, we propose an algorithm and the necessary assumption to estimate the attitude from a single temperature sensor and angular velocity measurements. This algorithm can be used in safe mode or as a fallback algorithm to obtain a valid attitude estimation despite a sensor failure. This work is the first contribution which introduces an observer that estimates the complete attitude of a spacecraft using only a single temperature measurement. It is based on the results of [12] and [13] which give the underlying observability analysis and attitude transformation of the observer.

The notations necessary to formulate the problem and the algorithm are introduced in Section II. In Section III, we present the non-linear model governing the thermal and attitude dynamics with only a single temperature sensor. A rigorous problem formulation is given in Section IV. Section V provides the background on conventional attitude estimations for spacecraft and illustrates the difficulty and differences to the analysed problem. In Section VI, the considered system is transformed into canonical observability form. The detailed observer design and its analysis can be found in Section VII. Finally, simulations are carried out in Section VIII to verify the approach and discuss the influence of measurement noise.

II. Notation

With $\mathcal{L}_f^n h(x)$ we denote the n-th Lie derivative of a differentiable function h with respect to the vector field f. The i-th unit vector of $\mathbb{R}^n$ is defined by e_i. The image of the function f is denoted by $\mathrm{im}(f)$. We denote by I_n and 0_n the identity and zero matrix of dimension n for $n \in \mathbb{N}$. We neglect the subscript n when the dimension of the matrix is clear. We use $0_{m,n}$ to denote the zero matrix of dimension $m \times n$ and we write $I_{m,n} = [I_m \, 0_{m,n-m}]$ for $m, n \in \mathbb{N}$ and $n > m$. For an $n \in \mathbb{N}$ dimensional vector x we denote by x_i the i-th component and by $x_{i:j} = [x_i \;\; x_{i+1} \;\; \dots x_j]$ the components i to j where $i < j \leq n$ and $i, j \in \mathbb{N}$.

Throughout this paper we use quaternions and their algebra to introduce the proposed attitude representation. Most of the notations are borrowed from [2]. Let

$$\mathbb{S}_i = \{x \in \mathbb{R}^{i+1} \mid \|x\| = 1\}$$

be the i-th unit sphere with $\|\cdot\|$ the Euclidean norm. We denote with $\mathcal{SO}_3$ the special orthogonal group

$$\mathcal{SO}_3 = \{A \in \mathbb{R}^{3\times 3} \mid AA^\top = I, \det(A) = 1\}$$

which contains all rotation matrices. Dependent on the context we denote with $q = \begin{bmatrix} q_1 & q_2 & q_3 & q_4 \end{bmatrix}^\top$ either a quaternion, i.e. $q \in \mathbb{S}_3$, or the function $q : \mathbb{S}_2 \times \mathbb{R} \to \mathbb{S}_3$ mapping a rotation vector $\rho \in \mathbb{S}_2$ and angle $\phi \in [-\pi, \pi)$ onto the corresponding quaternion, i.e.

$$q(\rho, \phi) = \begin{bmatrix} \rho_1 \sin(\frac{\phi}{2}) & \rho_2 \sin(\frac{\phi}{2}) & \rho_3 \sin(\frac{\phi}{2}) & \cos(\frac{\phi}{2}) \end{bmatrix}^\top .$$

The cross product matrix and the matrix required for quaternion multiplication are defined as

$$[u\times] = \begin{pmatrix} 0 & -u_3 & u_2 \\ u_3 & 0 & -u_1 \\ -u_2 & u_1 & 0 \end{pmatrix}, \quad \Xi(q) = \begin{pmatrix} q_4 I_3 + [q_{1:3}\times] \\ -q_{1:3}^\top \end{pmatrix}$$

for $u \in \mathbb{R}^3$ and $q \in \mathbb{S}_3$. In order to define the quaternion dynamics we also introduce for $\omega \in \mathbb{R}^3$ the matrix

$$\Omega(\omega) = \begin{pmatrix} -[\omega\times] & \omega \\ -\omega^\top & 0 \end{pmatrix} .$$

With A we denote the function which maps an attitude representation onto its rotation matrix allowing to transform a vector from one coordinate system into another. Throughout this paper we use for a rotation vector $\rho \in \mathbb{S}_2$, a rotation angle $\phi \in \mathbb{R}$ and for a quaternion $q \in \mathbb{S}^3$ the transformation into rotation matrix defined by

$$A(\rho, \phi) = \cos(\phi) I_3 - \sin(\phi)[\rho\times] + (1 - \cos(\phi))\rho\rho^\top$$
$$A(q) = \|q\|^{-2}\Big((q_4^2 - \|q_{1:3}\|^2) I_3 + 2 q_{1:3} q_{1:3}^\top - 2 q_4 [q_{1:3}\times]\Big) .$$

Any definition for $\rho \in \mathbb{S}_2$ is augmented for $\bar{\rho} \in \mathbb{R}^3$ by simply using $\rho = \frac{\bar{\rho}}{\|\bar{\rho}\|}$. For the inverse quaternion q^{-1} and the quaternion multiplication denoted by $\otimes$ we use

$$q^{-1} = [-q_{1:3}^\top, q_4]^\top \tag{1}$$
$$A(q)^{-1} = A(q)^\top \tag{2}$$
$$q \otimes \bar{q} = \begin{bmatrix} \Xi(\bar{q}) & \bar{q} \end{bmatrix} q \tag{3}$$
$$A(q \otimes \bar{q})^\top = A(\bar{q})^\top A(q)^\top . \tag{4}$$

Finally, we write asin, acos and atan2 to denote the inverse of the sine, cosine and tangent with the image $[-\frac{\pi}{2}, \frac{\pi}{2}]$, $[0, \pi]$ and $(-\pi, \pi]$, respectively.

III. System Dynamics

The overall system dynamics can be split into thermal and attitude dynamics.

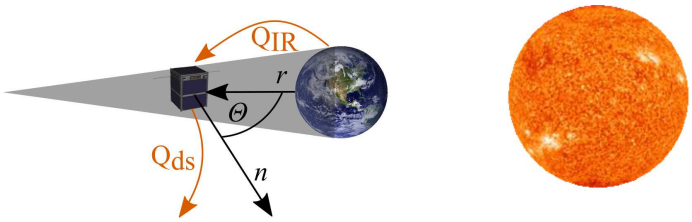

Fig. 1: Illustration of the considered system. Source of the Earth, Spacecraft and Sun image: NASA

A. Thermal Dynamics

We use the model and notations of [14] based on the work of [15] and [16]. The dynamics of the temperature are assumed to be governed solely by environmental heat. The dynamics have the form

$$\dot{T} = Q_{\text{sun}}(q,t) + Q_{\text{alb}}(q,t) + Q_{\text{IR}}(q,t) - Q_{\text{ds}}(T) \tag{5}$$

where $T(t) \in \mathbb{R}^+$ is the temperature, Q_{sun} is the solar, Q_{alb} the albedo, Q_{IR} the infrared and Q_{ds} the deep space irradiation which are dependent on the time $t \in \mathbb{R}$ and the normalised quaternions $q(t) \in \mathbb{S}_3$ which describe the attitude of the body frame of the spacecraft with respect to the world Earth-centered inertial (ECI) frame. These irradiations can be used to divide the state space to obtain a family of smooth vector fields which define six different cases discussed in [12]. In this work, we consider the case in which solar and albedo irradiations are not acting, i.e. $Q_{\text{sun}}(q,t) = Q_{\text{alb}}(q,t) = 0$. While this is not representative for all other cases, this particular case is highly relevant as it occurs periodically for example when the spacecraft is in the eclipse as illustrated in Fig. 1. Additionally, this case has the worst numerical observability properties as discussed in [12]. Further, the diminished complexity of this case allows an analytical design of methods. The augmentation of these methods on the other cases is subject of another work and will not be discussed here. The infrared irradiation is a function of the attitude and time defined by

$$Q_{\text{IR}}(q,t) = \gamma F(\theta(q,t), r(t)) \tag{6}$$

where $\gamma \in \mathbb{R}^+$ is a positive parameter and F a function dependent on the angle $\theta(q,t) \in [0,\pi]$ between the surface normal $n \in \mathbb{R}^3$ of the considered temperature sensor and the spacecraft position $r(t) \in \mathbb{R}^3$. The parameter γ is defined by

$$\gamma = \frac{1}{C}\varepsilon_{\text{e}} A_{\text{s}} I_{\text{IR}} \tag{7}$$

with the thermal capacitance C, the infrared emissivity of the surface ε_{e}, the area of the surface A_{s}, and the intensity of Earth infrared irradiation I_{IR}. These are all assumed to be constant and dependent on the coating of the sensor and the considered orbit. Note that a more accurate model would incorporate the intensity of the Earth infrared irradiation as a function of position and time. To simplify the analytic analysis, however, these dependencies are neglected as commonly assumed in literature, see e.g. [4], [8]. The function F denotes a form factor which models the irradiations between the spacecraft surface and the Earth. This form factor is defined by

$$F(\theta,r) = \begin{cases} \frac{\cos(\theta)}{H^2} & \theta \le \frac{\pi}{2} - \operatorname{asin}\left(\frac{1}{H}\right) \\ F_{\text{f},2} & \frac{\pi}{2} - \operatorname{asin}\left(\frac{1}{H}\right) < \theta < \frac{\pi}{2} + \operatorname{asin}\left(\frac{1}{H}\right) \\ 0 & \theta \ge \frac{\pi}{2} + \operatorname{asin}\left(\frac{1}{H}\right) \end{cases} \tag{8}$$

with $H = \frac{\|r\|}{r_\oplus}$ where $r_\oplus$ is the Earth mean radius and

$$\begin{aligned} F_{\text{f},2} = \frac{1}{2} - \frac{1}{\pi}\operatorname{asin}\left(\frac{\sqrt{H^2-1}}{H\sin(\theta)}\right) \\ + \frac{1}{\pi H^2}\Big(\cos(\theta)\operatorname{acos}\big(-\sqrt{H^2-1}\cot(\theta)\big) \\ - \sqrt{H^2-1}\sqrt{1-H^2\cos(\theta)^2}\Big). \end{aligned}$$

The angle $\theta(q,t)$ is defined by the attitude q and spacecraft position $r(t)$ as follows

$$\theta(q,t) = \operatorname{acos}\left(-\frac{r^\top(t)}{\|r(t)\|}A(q)^\top n\right) \in [0,\pi].$$

We model the position of the spacecraft r as a simple periodic function of time with

$$r_i(t) = a_i \sin(\omega_{\text{o}} t + b_i) \tag{9}$$

for constants $a_i, b_i \in \mathbb{R}$ and $i \in \{1,2,3\}$. Note that the orbits considered in this work admit $r(t) \neq 0$ for all t. The parameters are obtained by a fit of the position of the spacecraft which is obtained by a higher order gravity model [2]. The simplification using the sinusoidal approximation is reasonable because the considered simulation time is significantly smaller than the orbit time. Further, it allows us to analytically calculate the Lie derivatives required for the observability mapping. The deep space irradiation is defined as a function of the temperature as

$$Q_{\text{ds}}(T) = \delta T^4$$

with the parameter

$$\delta = \frac{1}{C}\varepsilon_{\text{e}} A_{\text{s}} \sigma$$

where σ is the Stefan-Boltzmann constant.

B. Attitude Dynamics

The quaternion dynamics defining the angle $\theta(q,t)$ are described by

$$\dot{q} = \frac{1}{2}\Omega(\omega) q \tag{10}$$

where $\omega \in \mathbb{R}^3$ is the angular velocity of the spacecraft, the dynamics of which are described by Euler's rotation equation

$$\dot{\omega} = J^{-1}(-\omega \times J\omega) + J^{-1}u \tag{11}$$

with inertia matrix $J \in \mathbb{R}^{3\times 3}$ and control input $u \in \mathbb{R}^3$.

C. Total Dynamics

The complete dynamics resulting from (5), (10) and (11) have the form

$$\dot{T} = \gamma F(\theta(q,t), r(t)) - \delta T^4 \tag{12a}$$
$$\dot{q} = \frac{1}{2}\Omega(\omega) q \tag{12b}$$
$$\dot{\omega} = J^{-1}(-\omega \times J\omega) + J^{-1}u \tag{12c}$$
$$\dot{t} = 1\,. \tag{12d}$$

Note that the time t is introduced as a state with the dynamics $\dot{t} = 1$. This is a common approach which increases the system dimension by one and induces new non-linearities. However, it has the advantage of rendering the system time-invariant and allowing to apply methods designed for time-invariant systems. The state vector has the form $x = \begin{bmatrix} T & q^\top & \omega^\top & t \end{bmatrix}^\top \in \mathbb{R}^9$ and is an element of the state space $\mathbb{X}$ which is a subset of $\mathbb{R}^+ \times \mathbb{S}_3 \times \mathbb{R}^3 \times \mathbb{R}$.

We close this section by introducing notation to render the problem statement more compact. Let the right-hand sides of the temperature dynamics be denoted by $f_T = \gamma F(\theta(q,t), r(t)) - \delta T^4$, of the quaternion dynamics by $f_q(q,\omega) = \frac{1}{2}\Omega(\omega)q$, of Euler's rotation equation by $f_\omega(\omega) = J^{-1}(-\omega \times J\omega)$ and $g_\omega = J^{-1}$, of the time dynamics by $f_t = 1$, and of the total dynamics as $f^\top = \begin{bmatrix} f_T & f_q^\top & f_\omega^\top & f_t \end{bmatrix}$ and $g^\top = \begin{bmatrix} 0 & 0 & g_\omega & 0 \end{bmatrix}$.

IV. Problem Statement

The objective of this work is to reconstruct the attitude using only a single temperature measurement with angular velocity measurements. This is equivalent to finding an observer of the system

$$\dot{x} = f(x) + gu \tag{13a}$$
$$y = h(x) \tag{13b}$$

with the output $y \in \mathbb{R}^6$ obtained using the output function $h : \mathbb{X} \to \mathbb{R}^6$ with

$$h^\top(x) = \begin{bmatrix} T & q^\top q - 1 & \omega^\top & t \end{bmatrix}^\top .$$

The dynamics (13a) are an abstract version of (12). The six dimensional output incorporates the temperature T, the angular velocity ω and the time t which can be measured. It is well known that the attitude space is of dimension three and that the quaternion representation uses four variables to allow a singularity-free representation. In order to ensure that the quaternion space is also only of order three despite being described by four variables it is restricted to unit quaternions. Thus, every quaternion q is an element of the unit sphere $\mathbb{S}_3$ and this is accounted for by adding a virtual output $q^\top q - 1$. This output variable can be omitted if the observer structure inherently guarantees that the quaternion constraint is fulfilled or it can be used, as suggested here, as an additional output which is constant zero (and does not need to be measured). In this work, as an observer of system (13) we consider any system

$$\dot{\hat{x}} = f(\hat{x}) + gu + L(\hat{x}, y, \hat{y}) \tag{14a}$$
$$\hat{y} = h(\hat{x}) \tag{14b}$$

such that the estimate $\hat{x}$ is the real state x if the initial state is known, i.e. for all t holds $\hat{x}(t) = x(t)$ if $\hat{x}(0) = x(0)$. Additionally, the estimate $\hat{x}$ of an observer must converge to the real state x for any initial value, i.e. $\lim_{t\to\infty} \|\hat{x}(t) - x(t)\| = 0$. Note that (14) consists of the same dynamics as (13), but with an additional correction term $L(\hat{x}, y, \hat{y})$ which usually incorporates the error between the measured and the estimated output.

V. Comparison to State of the Art Algorithms

Commonly, the attitude of a spacecraft is obtained using approaches that depend on multiple vector measurements taken at the same time [2]. This can be considered as a static optimisation problem known as *Wahba's problem* [17] which minimises the loss function

$$\frac{1}{2}\sum_{i=1}^{N} \alpha_i \|n^i - Ar^i\|$$

over the attitude matrix $A \in \mathcal{SO}_3$ for the gains $\alpha_i \in \mathbb{R}^+$, the vector measurements in ECI and body frame $n^i, r^i \in \mathbb{R}^3$ for $i \in \{1, \ldots, N\}$ and the number of measurements $N \geq 2$. Different algorithms exist to ensure an optimal solution of this problem, as presented e.g. in [2]. Another method commonly employed is to incorporate the vector measurements in an observer design. Multiplicative extended Kalman filters use quaternions as a global attitude representation while the local representation of attitude is achieved using a three dimensional attitude description. The global attitude error is incorporated in a multiplicative fashion. In our case, if multiple temperature measurements T^1,T^2, ... T^N were available, as it is the case for e.g. industrial Coarse Earth Sun Sensors, it would be possible to use one of these two methods. But since only a single measurement is available, it is not straightforward to apply these algorithms because we need to rely on higher order derivatives of the temperature. A commonly employed first approach would be to use an observer scheme that relies on a linearisation of the system for the estimation.

We illustrate why it is not advisable to apply such a linearisation for the proposed system class with quaternions. First, a linearisation of the quaternion dynamics leads to the system matrix $\frac{1}{2}\Omega(\omega)$ with all eigenvalues located on the imaginary axis. Thus, every equilibrium point is not hyperbolic and the Hartmann-Grobman theorem does not guarantee the existence of a homeomorphism between the linearisation and the original dynamics. Further, the quaternion space $\mathbb{S}_3$ is not euclidean and a trajectory that obeys the dynamics of the linearisation leaves the quaternion space. Instead, we use a non-linear approach in which we transform the system into canonical observability form which allows to design an observer without the use of a linearisation.

VI. Transformation into Canonical Form

Based on (13b), define the transformation $\mathcal{O}$ of the form

$$\begin{aligned}\mathcal{O}:\ &\mathbb{R}^+\times\mathbb{S}_3\times\mathbb{R}^3\times\mathbb{R}\to\mathbb{R}^+\times\mathbb{R}\times\mathbb{R}\times\mathbb{R}\times\{0\}\times\mathbb{R}^3\times\mathbb{R}^+\\ &x=(T,q,\omega,t)\mapsto\mathcal{O}(x)=z\end{aligned}\tag{15}$$

with the new coordinate $z\in\mathbb{R}^9$ defined by

$$z=[T,\mathcal{L}_f^1h(x),\mathcal{L}_f^2h(x),\mathcal{L}_f^3h(x)+\mathcal{L}_g\mathcal{L}_f^2h(x)u,q^\top q-1,\omega^\top,t]^\top$$

where $z_{1:4}$ are the temperature and its first three derivatives, z_5 is the quaternion constraint, $z_{6:8}$ the angular velocity and z_9 the time. The expressions for the Lie derivatives can be found in Appendix A. Note that the transformation consists only of the outputs and their derivatives. This transformation is also an observability mapping in the spirit of [18] to identify the observability properties of the system (13) as utilised in [12]. Roughly speaking, the system is *globally observable* if the mapping $\mathcal{O}$ is bijective because this allows to map the state z, consisting only of measured outputs y and its (estimated) time derivatives $y^{(i)}$, to exactly one state x. This means, injectivity ensures that for each measured temperature and its time derivatives there exists at most one attitude q. This forbids the existence of multiple attitudes generating the same temperature evolution. Surjectivity on the other hand ensures that for every temperature and its derivatives there exists at least one attitude. This guarantees that even under the influence of measurement disturbances an estimate of the attitude can be obtained. In [12], we have already shown that this kind of *global observability* does not hold as there are points for which the Jacobian of the observability mapping does not have full rank. *Weak observability*, however, in this contribution was shown to hold for most of the states. This ensures at least local invertibility of the observability mapping $\mathcal{O}$. To be more specific, consider a point x for which weak observability is ensured. Then, there exist neighbourhoods $U(x)$ of x and $V(\mathcal{O}(x))$ of $\mathcal{O}(x)$ such that there is a local inverse $\mathcal{O}^{-1}:V(\mathcal{O}(x))\to U(x)$ which fulfils $\mathcal{O}^{-1}(\mathcal{O}(x))=x$. For such a point the transformed dynamics are in observability canonical form

$$\dot z=\begin{bmatrix}0_{3,1}&I_{3,8}\\0_{1,1}&0_{1,8}\\0_{1,1}&0_{1,8}\\0_{3,1}&0_{3,8}\\0_{1,1}&0_{1,8}\end{bmatrix}z+\begin{bmatrix}0_{3,1}\\\varphi_4(z)\\\varphi_5(z)\\\varphi_{6:8}(z_{6:8})\\\varphi_9(z_9)\end{bmatrix}+\begin{bmatrix}0_{3,3}\\\phi_5(z)\\0_{3,3}\\J^{-1}\\0_{3,3}\end{bmatrix}u\tag{16a}$$

$$y=\begin{bmatrix}z_1\\z_5\\z_{6:8}\\z_9\end{bmatrix}\tag{16b}$$

with the non-linear functions

$$\begin{aligned}\varphi_4(z)&=\mathcal{L}_f^{(4)}h(x)|_{x=\mathcal{O}^{-1}(z)}\\\varphi_5(z)&=q^\top\Xi(q)\omega|_{x=\mathcal{O}^{-1}(z)}\\\varphi_{6:8}(z)&=f_\omega(z_{6:8})\\\varphi_9(z)&=1\\\phi_5(z)&=\mathcal{L}_g\mathcal{L}_f^{(3)}h(x)|_{x=\mathcal{O}^{-1}(z)}\,.\end{aligned}$$

This system has six outputs where each of them forms a differentiator subsystem with the non-linearity only occurring in the final derivative. The non-linearities $\varphi_{6:8}$ and φ_9 are known and functions of the output while the non-linearities φ_4, φ_5 and ϕ_5 can only be approximated numerically and are also functions of the approximated states and not only of the measured output. This system in canonical form can now be used to estimate the desired states. Here we shall emphasise that using the required third order derivative of the temperature requires a very high accuracy of the governing model equations and of the measurements. Conventional temperature sensors have an accuracy of about 0.1°C and a sampling frequency of 1Hz [19], [20] and model accuracies vary with orbit and time. A thorough robustness analysis of these aspects is beyond the scope of this work in which the focus lies on the reconstruction in the disturbance free case.

VII. Observer Design

There are two approaches which come immediately into one's mind that utilise the canonical form to design an observer. Among others, these are also used in [18]. In the first approach an observer is designed for the transformed z coordinates. In our case such an observer can be chosen as

$$\dot{\hat z}=\begin{bmatrix}0_{3,1}&I_{3,8}\\0_{1,1}&0_{1,8}\\0_{1,1}&0_{1,8}\\0_{3,1}&0_{3,8}\\0_{1,1}&0_{1,8}\end{bmatrix}\hat z+\begin{bmatrix}0_{3,1}\\\varphi_4(\hat z)\\\varphi_5(\hat z)\\\varphi_{6:8}(\hat z_{6:8})\\\varphi_9(\hat z_9)\end{bmatrix}+\begin{bmatrix}0_{3,3}\\\phi_5(\hat z)\\0_{3,3}\\J^{-1}\\0_{3,3}\end{bmatrix}u+L(y-\hat y)\tag{17a}$$

$$\hat y=\begin{bmatrix}\hat z_1\\\hat z_5\\\hat z_{6:8}\\\hat z_9\end{bmatrix}\tag{17b}$$

with the correction term

$$L(y-\hat y)=\begin{bmatrix}L_{1:3}(y_1-\hat y_1)\\L_4(y_1-\hat y_1)\\L_5(y_2-\hat y_2)\\L_{6:8}(y_{3:5}-\hat y_{3:5})\\L_9(y_6-\hat y_6)\end{bmatrix}=\begin{bmatrix}L_{1:3}(z_1-\hat z_1)\\L_4(z_1-\hat z_1)\\L_5(z_5-\hat z_5)\\L_{6:8}(z_{6:8}-\hat z_{6:8})\\L_9(z_9-\hat z_9)\end{bmatrix}$$

where L_i can be a matrix of numbers or some non-linear function for $i\in\{1,\dots,6\}$. We call such an observer *differentiator*, because it is designed for a system in canonical form where the states are explicit functions of the outputs and their derivatives. Then a transformation into the original x coordinates is used, i.e.

$$\hat x=\mathcal{O}^{-1}(\hat z)\tag{18}$$

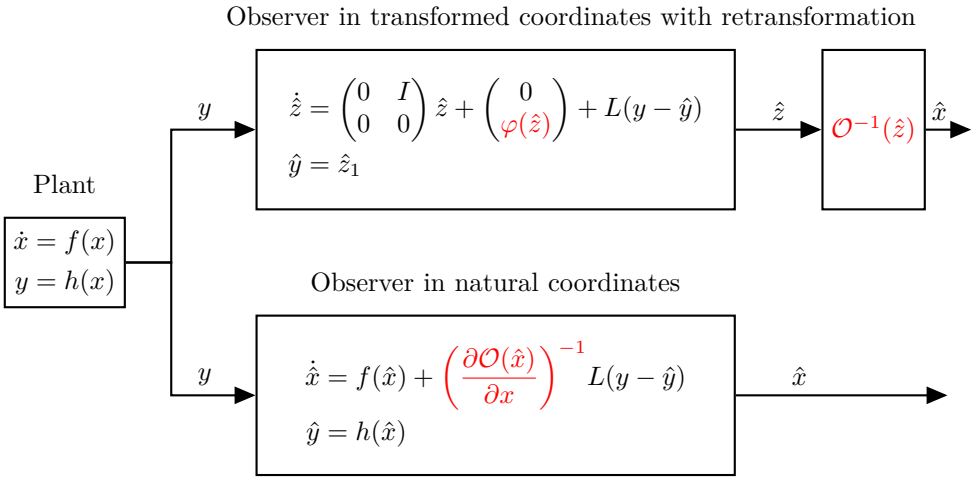

Fig. 2: Two observer schemes using the transformation into canonical form $\mathcal{O}$ for an autonomous system

which utilises the local inverse of $\mathcal{O}$. The existence of the local inverse is dependent on the current state x and discussed in detail in [12].

The second approach designs an equivalent observer directly in original coordinates. By differentiating (18), with $\frac{\partial \mathcal{O}^{-1}(z)}{\partial z} = \left(\frac{\partial \mathcal{O}(x)}{\partial x}\right)^{-1}$ we obtain the observer

$$\dot{\hat{x}} = f(\hat{x}) + g(\hat{x})u + \left(\frac{\partial \mathcal{O}(\hat{x})}{\partial x}\right)^{-1} L(y - \hat{y})\,. \tag{19}$$

This observer has the benefit that it uses the inverse of the Jacobian of $\mathcal{O}(x)$ instead of the inverse of the mapping $\mathcal{O}$ which is difficult to obtain in closed terms.

Fig. 2 illustrates the two different possibilities to construct the observer using the transformation into canonical form. The two approaches are equivalent and for both inversion and differentiation are necessary. The difficulty of the first approach lies in determining φ and $\mathcal{O}^{-1}$. Often, instead of numerically calculating φ, it is neglected in the observer design and compensated by a suitable choice of L. The inverse $\mathcal{O}^{-1}$ is usually obtained via solving an optimisation problem. For the second approach the Jacobian of $\mathcal{O}$ needs to be calculated and inverted. This is in general numerically less costly than the first approach. Both approaches have their limitations if $\mathcal{O}$ is not bijective. In the first approach, φ and $\mathcal{O}^{-1}$ are not uniquely defined any more and the resulting estimation depends on the choice of these functions. In the second approach $\left(\frac{\partial \mathcal{O}(\hat{x})}{\partial x}\right)^{-1}$ does not exist for some $\hat{x}$ and the estimation depends on the initial values of $\hat{x}$. In this work we adhere to the spirit of the first approach as it allows a strict separation between the differentiation and inversion task. The algorithm is illustrated in the block diagram in Fig. 3.

A. Differentiation

We use (17) as a basis to design a differentiator that estimates the transformed states z. The main task is to choose $L_{1:4}$ which can be considered as finding a suitable algorithm to differentiate z_1. Many different methods such as linear differentiators, high gain differentiators [21] or sliding mode differentiators [22] enable to estimate such derivative. We have decided to use a high gain differentiator as in [21] since these kind of observers provide a rapid and exact estimate if their gain tends to infinity. This can be used to omit the functions φ_4, ϕ_5 and renders $L_{1:4}$ a column vector $L_{1:4} \in \mathbb{R}^4$. The observer is then given by

$$\dot{\hat{z}}_{1:4} = \begin{pmatrix} 0 & 1 & 0 & 0 \\ 0 & 0 & 1 & 0 \\ 0 & 0 & 0 & 1 \\ 0 & 0 & 0 & 0 \end{pmatrix} \hat{z}_{1:4} + \begin{pmatrix} \frac{\alpha_0}{\varepsilon} \\ \frac{\alpha_1}{\varepsilon^2} \\ \frac{\alpha_2}{\varepsilon^3} \\ \frac{\alpha_3}{\varepsilon^3} \end{pmatrix} (y_1 - \hat{y}_1) \tag{20a}$$

$$\hat{y}_1 = \hat{z}_1 \tag{20b}$$

where $\varepsilon > 0$ is sufficiently small and the parameters α_0, α_1, α_2 and α_3 are chosen such that the corresponding polynomial $s^4 + \alpha_3 s^3 + \alpha_2 s^2 + \alpha_1 s + \alpha_0$ is Hurwitz.

The quaternion constraint z_5 is a virtual output and identical to zero, i.e.

$$\hat{z}_5 \equiv 0\,. \tag{21}$$

In the next section a transformation will be introduced that incorporates this constraint. Thus, calculating ϕ_5 and designing L_5 is not necessary.

The angular velocity $z_{6:8}$ is directly measured which allows to choose $L_{6:8} = \operatorname{diag}(\lambda_6, \lambda_7, \lambda_8)$ as diagonal matrix and

$$\dot{\hat{z}}_{6:8} = \varphi_{6:8}(\hat{z}_{6:8}) + J^{-1}u + \operatorname{diag}(\lambda_6, \lambda_7, \lambda_8)(y_{3:5} - \hat{y}_{3:5}) \tag{22a}$$

$$\hat{y}_{3:5} = \hat{z}_{6:8} \tag{22b}$$

with suitable design parameters $\lambda_6, \lambda_7, \lambda_8 \in \mathbb{R}^+$ to achieve asymptotic stability and the desired filtering properties.

Since the time z_9 is known, we do not use the proposed filtering dynamics, but we use

$$\hat{z}_9 = y_6 \tag{23}$$

instead and do not require to choose L_9. Equations (20), (21), (22) and (23) form the desired differentiator and are illustrated in Fig. 3.

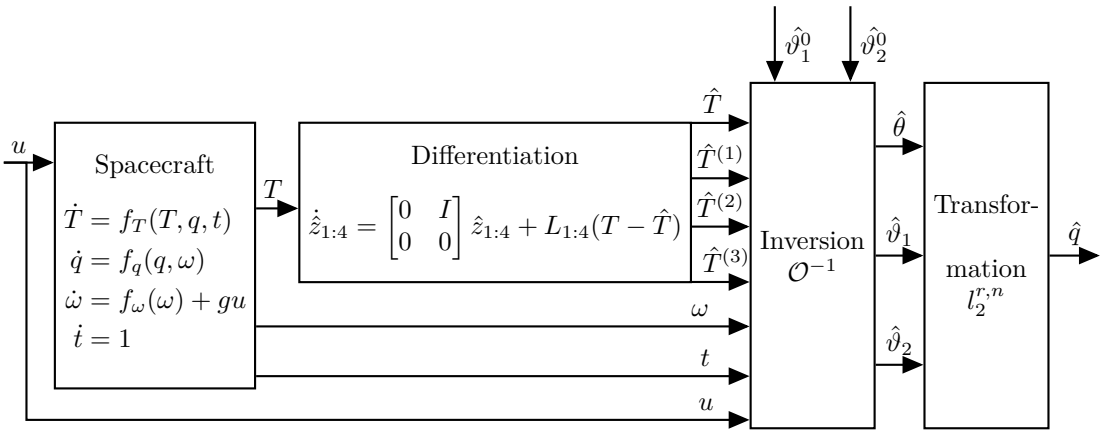

Fig. 3: Attitude reconstruction using differentiation and an inversion with transformation

B. Inversion

In this section we analyse the function $\mathcal{O}$ and propose a way to obtain the original state x through the inversion of (15) for given measurements and estimated derivatives gathered in z. This is achieved by proposing a transformation from quaternions into a set of three angles describing the attitude while also having an immediate relation to the acting flux. Then the inversion problem is formulated into an optimisation problem and the points impairing the injectivity are identified.

The measured temperature is described by $z_1 = y_1$. The output $z_5 = y_2$ is the quaternion constraint identical to zero, the output $z_{6:8} = y_{3:5}$ is the angular velocity and $z_9 = y_6$ is the time t. We use this to define the functions $L_2^{T,\omega,t}(q) := \mathcal{L}_f^{(2)} h(x)$ and $L_3^{T,\omega,t,u}(q) := \mathcal{L}_f^{(3)} h(x) + \mathcal{L}_g \mathcal{L}_f^2 h(x) u$. Then, we can remove the trivial parts of (15) and obtain the function of interest

$$\begin{aligned} \mathcal{O}_{2:5}^{T,\omega,t} &: \mathbb{S}_3 \to \mathbb{R} \times \mathbb{R} \times \mathbb{R} \times \{0\} \\ q &\to \mathcal{O}_{2:5}^{T,\omega,t}(q) = (z_2, z_3, z_4, z_5) \end{aligned} \tag{24}$$

where the image is defined by the non-linear algebraic system of equations

$$z_2 = \gamma F(\theta(q,t), r(t)) - \delta T^4 \tag{25a}$$
$$z_3 = L_2^{T,\omega,t}(q) \tag{25b}$$
$$z_4 = L_3^{T,\omega,t,u}(q) \tag{25c}$$
$$z_5 = q^\top q - 1\,. \tag{25d}$$

1) Reduction of the Order of the System: This system is highly non-linear and the existence as well as the uniqueness of a solution are not clear. One main problem is the non-euclidean structure of the quaternion space and the fact that there is no straightforward way to isolate one of the variables to reduce the order of the system.

Thus, we introduce a transformation l_1 which maps each quaternion to a set of angles $(\theta, \vartheta_1, \vartheta_2)$ such that the first angle θ can be directly obtained from (25a). The transformation and its inverse transformation are introduced in the following theorem.

Theorem VII.1 *For $r, n \in \mathbb{S}_2$ consider the transformation*

$$\begin{aligned} l_1^{r,n} &: \mathbb{S}_3 \to [0, \pi] \times (-\pi, \pi] \times (-2\pi, 2\pi] \\ q &\mapsto l_1^{r,n}(q) = (\theta, \vartheta_1, \vartheta_2) \end{aligned}$$

the image of which is defined by

$$\theta = \operatorname{acos}(r^\top A(q) n)$$
$$\vartheta_1 = \operatorname{atan2}((r \times n^{\theta,0})^\top n^q, {n^{\theta,0}}^\top n^q - (r^\top n^{\theta,0})^2)$$
$$\vartheta_2 = \begin{cases} +2\operatorname{acos}(\bar{q}_4) & \frac{\bar{q}_{1:3}}{\|\bar{q}_{1:3}\|} = n^q \\ -2\operatorname{acos}(\bar{q}_4) & \frac{\bar{q}_{1:3}}{\|\bar{q}_{1:3}\|} = -n^q \end{cases}$$

with the two rotation axes defined by $n^q = A(q)^\top n$, $n^{\theta,0} = A\left(e_i \times r, \theta\right)^\top r$ and the quaternion which is describing the rotation around the n^q axis as $\bar{q} = q^{-1}(r, \vartheta_1) \otimes q^{-1}\left(e_i \times r, \theta\right) \otimes q^{-1}(v, \phi) \otimes q$ with the rotation axis $v = \frac{n \times r}{\|n \times r\|}$ and angle $\phi = \operatorname{acos}(n^\top r)$.

The inverse transformation $l_2^{r,n}$ has the form

$$\begin{aligned} l_2^{r,n} &: [0, \pi] \times (-\pi, \pi] \times (-2\pi, 2\pi] \to \mathbb{S}_3 \\ &(\theta, \vartheta_1, \vartheta_2) \mapsto l_2^{r,n}(\theta, \vartheta_1, \vartheta_2) \end{aligned}$$

where the image is defined by

$$l_2^{r,n}(\theta, \vartheta_1, \vartheta_2) = q(v, \phi) \otimes q(e_i \times r, \theta) \otimes q(r, \vartheta_1) \otimes q(n^{\theta, \vartheta_1}, \vartheta_2)$$

with the rotation axis $n^{\theta,\vartheta_1} = A(r, \vartheta_1)^\top A(r \times e_i, \theta)^\top r$.

Then $l_1^{r,n}$ is the inverse of $l_2^{r,n}$ for $\theta \notin \{0, \pi\}$ and vice versa.

Proof: The derivation of the transformation and its properties are given in [13]. ∎

The main advantage of the representation $(\theta, \vartheta_1, \vartheta_2)$ is that its domain is euclidean and that its first variable describes the angle between r and n which can be used to reduce the order of the non-linear system. The second and third variable ϑ_1 and ϑ_2 both correspond to rotations which are visualised in [13]. However, their interpretation is less straightforward than that of θ as previous rotations are required to be performed beforehand. With this transformation we can rewrite system (25) in $(\theta, \vartheta_1, \vartheta_2)$

coordinates to obtain

$$z_2 = \gamma F(\theta, r(t)) - \delta T^4 \tag{26a}$$
$$z_3 = L_2^{T,\omega,t}(l_2^{r,n}(\theta, \vartheta_1, \vartheta_2)) \tag{26b}$$
$$z_4 = L_3^{T,\omega,t,u}(l_2^{r,n}(\theta, \vartheta_1, \vartheta_2)) \tag{26c}$$
$$z_5 = l_2^{r,n}(\theta, \vartheta_1, \vartheta_2)^\top l_2^{r,n}(\theta, \vartheta_1, \vartheta_2) - 1\,. \tag{26d}$$

As can be seen in (24), z_5 is identical to zero. Consequently, (26d) is fulfilled for any set of angles because the image of $l_2^{n,r}$ is the unit sphere. Additionally, it can be seen that the angle θ can be directly determined from (26a) because the form factor F is strictly monotonic. For $F(\theta, r(t)) = \frac{r_\oplus^2}{\|r\|^2}\cos(\theta)$ the angle can even be obtained analytically from (26a) as

$$\theta = \operatorname{acos}\left(\frac{1}{\gamma}\frac{\|r\|^2}{r_\oplus^2}(z_2 + \delta T^4)\right)\,. \tag{27}$$

This reduces (26) to the two non-linear equations

$$z_3 = H_3(\vartheta_1, \vartheta_2) \tag{28a}$$
$$z_4 = H_4(\vartheta_1, \vartheta_2) \tag{28b}$$

with the definitions $H_3(\vartheta_1, \vartheta_2) = L_2^{T,\omega,t}(l_2^{r,n}(\theta, \vartheta_1, \vartheta_2))$ and $H_4(\vartheta_1, \vartheta_2) = L_3^{T,\omega,t,u}(l_2^{r,n}(\theta, \vartheta_1, \vartheta_2))$. As this is a highly non-linear system of equations it is not possible to give an analytical expression for ϑ_1, ϑ_2 as a function of z. On top of that, this expression varies with the other states T, ω, t, θ and the parameters. In the next section we reformulate the non-linear system of equations (28) into an optimisation problem and discuss its solution for the parameters and states shown in Table II and III.

2) Formulation of the Optimisation Problem: We formulate the inversion problem (28) as the equivalent optimisation problem of the form

$$\min_{\vartheta_1,\vartheta_2} \quad \left\| \begin{matrix} H_3(\vartheta_1, \vartheta_2) - z_3 \\ H_4(\vartheta_1, \vartheta_2) - z_4 \end{matrix} \right\|_2 \tag{29a}$$
$$\text{s.t.} \quad [\vartheta_1, \vartheta_2] \in D_1 \times D_2 \tag{29b}$$

where D_1 and D_2 are the domains of ϑ_1 and ϑ_2, usually chosen to be an interval of length 2π. It is straightforward to see that every solution of (28) is a solution of (29) and vice versa. Plotting the image of the cost function of (29) allows to get an insight to the difficulty of this optimisation problem. Fig. 4 shows this image in the $(\vartheta_1, \vartheta_2)$-space for $[z_3, z_4] = [H_3(0,0), H_4(0,0)]$ and the given parameters and states. It can be seen that most of the level sets are approximately parallel to the ϑ_1 axis. However, there are two valleys with locally decreasing level sets. One contains the expected optimum while the other has a similar shape and seemingly multiple optima as well. Furthermore, the cost function varies barely for varying ϑ_1. This makes the determination of a solution difficult because all values along this manifold are optimal results under certain tolerances which will make the optimisation stop if a point $(\vartheta_1, 0)$ with $\vartheta_1 \in (-\pi, \pi]$ is reached. In order to avoid this issue, we need to transform the cost function to remove the slowly varying manifold. A simple linear transformation is proposed by considering the Taylor expansion of first order at the point $(\vartheta_1^*, \vartheta_2^*)$

$$H_{3:4}(\vartheta_1, \vartheta_2) \approx H_{3:4}(\vartheta_1^*, \vartheta_2^*) + \frac{\partial H(\vartheta_1^*, \vartheta_2^*)}{\partial(\vartheta_1, \vartheta_2)}\left(\begin{bmatrix}\vartheta_1 \\ \vartheta_2\end{bmatrix} - \begin{bmatrix}\vartheta_1^* \\ \vartheta_2^*\end{bmatrix}\right).$$

Reshaping the optimisation problem (29) using the Jacobian leads to a better conditioned problem of the form

$$\min_{\vartheta_1,\vartheta_2} \quad \left\| \left[\frac{\partial H(\vartheta_1, \vartheta_2)}{\partial(\vartheta_1, \vartheta_2)}\right]^{-1} \begin{bmatrix} H_3(\vartheta_1, \vartheta_2) - z_3 \\ H_4(\vartheta_1, \vartheta_2) - z_4 \end{bmatrix} \right\|_2 \tag{30a}$$
$$\text{s.t.} \quad [\vartheta_1, \vartheta_2] \in D_1 \times D_2\,. \tag{30b}$$

The image of this cost function is shown in Fig. 5. It has a smooth behaviour in the domain. The form of the level sets have changed significantly through the transformation. The attitude $(\vartheta_1, \vartheta_2) = 0$ used to determine the outputs now describes a minimum with near circular level sets in its vicinity. This is a desirable property with respect to numerically solving the optimisation problem. Additionally, it can be seen that there are multiple other minima. Some of them are due to the boundedness of the domain and can be found at its boundary. They can clearly be identified as non-global minima. Others, which can be found in the interior of the domain, exhibit a cost function value in the same range as for $(\vartheta_1, \vartheta_2) = 0$.

These minima show that the function $\mathcal{O}$ is not bijective for all x. For such x, this gives rise to a family of local inverse functions $\mathcal{O}_i^{-1} : V(\mathcal{O}(x)) \to U_i(\bar{\vartheta}_i)$ for $i \in \{1, \ldots, n_{\text{gm}}\}$ with $n_{\text{gm}} \in \mathbb{N}$ defined as the maximal number of global minima of the optimisation problem (30). The domain of these functions is identical while each range $U_i \subset \mathbb{X}$ is a neighbourhood defined by an other global minimum $\bar{\vartheta}_i$. The function values $\mathcal{O}_i^{-1}(z)$ are obtained solving the optimisation problem (30) for initial values in the basin of attraction of the different $\bar{\vartheta}_i$. Note that in particular $\mathcal{O}_i^{-1}(\mathcal{O}(x)) \neq \mathcal{O}_j^{-1}(\mathcal{O}(x))$ for $i \neq j$ for almost all x and that for at least one i holds $\mathcal{O}_i^{-1}(\mathcal{O}(x)) = x$.

3) The Global Minima and their Region of Attraction: As pointed out in the previous section, there exist multiple points that solve the optimisation problem locally. This makes the solution of the optimisation problem dependent on the optimisation method and the initial value. Local minima can be identified by having non-zero cost function values. If the solver converges to such a minimum, another initial value has to be used. Global minima can only be distinguished from the real solution by incorporating additional constraints into the optimisation problem. We identify the points to which the solver is converging and determine the basin of attraction of the global minima. For a compact notation $\vartheta = (\vartheta_1, \vartheta_2)$ is introduced.

The optimisation problem (30) is solved for a number of initial values that are uniformly covering the ϑ-space $[-\pi, \pi] \times [-\pi, \pi]$ with a gradient based solver. As in [23], using the optimisation result $\bar{\vartheta}$ we define the function

$$\mathcal{LS} : [-\pi, \pi] \times [-\pi, \pi] \to \operatorname{im}(\mathcal{LS}) \tag{31a}$$
$$\vartheta \mapsto \mathcal{LS}(\vartheta) = \bar{\vartheta} \tag{31b}$$

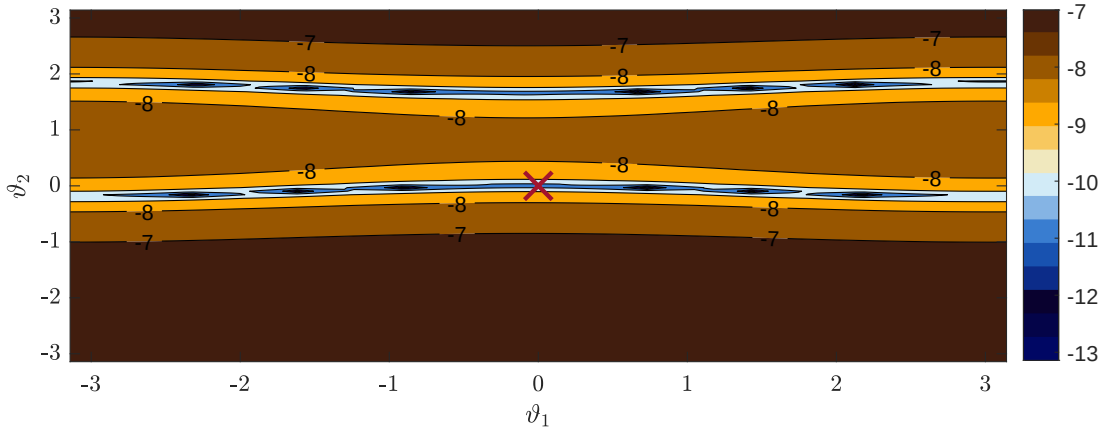

Fig. 4: Logarithmic visualisation of the cost function of optimisation problem (29) for $[z_3, z_4] = [H_3(0,0), H_4(0,0)]$.

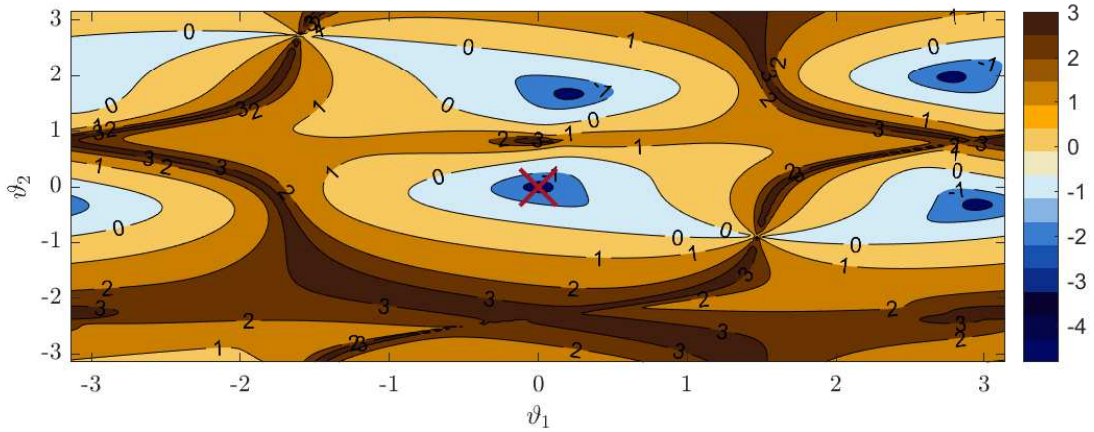

Fig. 5: Logarithmic visualisation of the cost function of optimisation problem (30) for $[z_3, z_4] = [H_3(0,0), H_4(0,0)]$.

mapping every initial value ϑ to the point $\bar{\vartheta}$ to which the solver is converging. It is clear that every point $\bar{\vartheta} \in \mathrm{im}(\mathcal{LS})$ is a global minimum if the cost function of $\bar{\vartheta}$ is equal to zero. In Table I the calculated points $\bar{\vartheta}$ and their costs are listed. There are four points with a cost very close to zero which identifies them as global optima. Four other points can be clearly identified as non-global optima by their higher value of the cost function. We define the basin of attraction of a minimum $\Lambda(\bar{\vartheta})$ as the pre-image of $\bar{\vartheta}$ under $\mathcal{LS}$, i.e.

$$\Lambda(\bar{\vartheta}) = \{\vartheta \in [-\pi, \pi] \times [-\pi, \pi] \mid \mathcal{LS}(\vartheta) = \bar{\vartheta}\}\,.$$

This basin is displayed for the individual minima $\bar{\vartheta} \in \mathrm{im}(\mathcal{LS})$ in Fig. 6. The global minima are marked by black crosses each lying in its basin of attraction. In red, the union of the initial values that do not converge to a global minimum can be seen. The green region displays the basin of attraction of $\bar{\vartheta} = [0, 0]^\top$ which was used for constructing the optimisation problem. The remaining colours correspond to the other three global minima. It can be seen that every minimum has a basin of attraction of reasonable size. Most parts of the basins of attraction are connected and clearly distinguishable. However, there are few points in each basin that make the smallest convex sets in the basins very conservative. The basin in which the initial value of the optimisation lies defines which inverse mapping $\mathcal{O}_i^{-1}$ is used. Note that the number and form of the basins of attractions vary decisively with the considered states (T, θ, ω, t). In particular, analyses have shown that the dependency on the angular velocity ω is complex and requires extensive analytical as well as numerical investigations which are out of scope for this work. However, it shall be emphasised that, as pointed out in [12], it is required to have $\omega \neq 0$ to allow for an estimation of the complete attitude.

We finish this section by stating the main assumption that allows to estimate the desired attitude with the proposed optimisation.

Assumption 1 *The initial value $\hat{\vartheta}^0(t)$ used for the optimisation algorithm* (30) *lies in the basin of attraction $\Lambda(\vartheta(t))$ of the current state $\vartheta(t)$ for every time $t \in \mathbb{R}$.*

In practical applications, this assumption can be fulfilled at the beginning of a failure mode because the last correct attitude estimate can be used for the optimisation. When no knowledge about a suitable initial value is available, it

is required to carry out the algorithm for multiple initial values as illustrated in the next section.

VIII. Simulation

In this section we simulate the algorithm presented in the previous section as illustrated in Fig. 3 for a spacecraft on a Sun-synchronous orbit with an altitude of 600km, with 06 : 00 longitude of the ascending node and an orbit period of about 97 min. The orbit is obtained using a model incorporating the first zonal coefficient and a fit to the polynomial (9). The parameters, constants and initial values can be found in Table II and III. Note that a Sun-synchronous orbit is an orbit whose orientation with respect to the Sun is similar over the complete year. A more detailed description about its properties and the required initial states can be found in [2]. The initial and simulation time is chosen such that the spacecraft is in solar eclipse, i.e. only infrared irradiation is acting on a spacecraft surface and the model (12) is valid. The spacecraft is assumed to have non-zero angular velocity and to be in a failure mode in which it is not controlled.

A. Ideal Measurements

In this section we neglect any measurement noise to put the focus on the loss of uniqueness of the solution and not on the estimation error or delay induced by noise. Therefore, we also incorporate directly the angular velocity measurement instead of filtering it. The integration is carried out using a Runge–Kutta solver with a fixed step size of 1s. The step size is chosen to be in the range of conventional temperature sensor sampling times [19], [20]. A high-gain differentiator as in (20) is used with the parameters $\alpha = \begin{bmatrix}8 & 24 & 32 & 16\end{bmatrix}$ and $\varepsilon = 2$. These parameters are chosen by hand and high when compared to literature so as to avoid numerical instabilities induced by the large simulation step size. A set of optimised parameters can be found in the next section. The inversion is realised solving the optimisation problem (30) at every time step using the simplex algorithm of the in-house DLR software MOPS [24]. Other methods using for example polynomial approximations as in Gloptipoly [25] have currently not been investigated, but will be considered in future research. In order to obtain continuous solutions, we use the attitude of the previous step as the initial value of the current step for the optimisation. Further the domains D_1 and D_2 of ϑ_1 and ϑ_2 are moved with the last estimation, i.e. $D_1(t_{k+1}) = \vartheta_1(t_k) + [-\pi, \pi]$ and $D_2(t_{k+1}) = \vartheta_2(t_k) + [-\pi, \pi]$. Note that carrying out the optimisation is computationally very expensive. In its current state the optimisation is not real-time applicable which will make modifications of the optimisation or the developed algorithms necessary in future work if an online estimation is desired.

Since Assumption 1 is essential for the algorithm, we show two simulations. The first one has a simulation time of 100 s during which the assumption holds. The second simulation has the same setup as the first one, but has a longer simulation time during which the assumption is not fulfilled anymore. Additionally, estimates of initial values in different basins of attractions not fulfilling the assumption are displayed.

1) The Assumption holds: The algorithm illustrated in (30) consists mainly of two steps, namely the differentiation of the temperature data and the estimation of the attitude from the estimated temperature and its derivatives. Fig. 7 shows the estimation errors of the temperature and its derivatives. As expected for a high gain observer, the peaking phenomenon occurs. Thus, in the transient phase between 0 and 5 seconds (recall step size of 1 s), the estimation error is large. Afterwards, it can be seen that desired derivatives are estimated with a sufficiently small error. In Fig. 8 the estimation errors of the angles $(\theta, \vartheta_1, \vartheta_2)$ for the initial values $(\theta^0, \vartheta_1^0(0)\vartheta_2^0(0)) = (2, -0.5, 0.5)$ are presented. During the transient phase of the differentiator, the optimisation is not carried out and simply the initial value is held. After the transient phase the optimisation converges and follows the real attitude with small numerical errors.

2) The Assumption does not hold: In order to illustrate the importance of Assumption 1, we determine the solution over time for four initial values. Each of these initial values lies in another basin of attraction of the existing global minima displayed in Fig. 5. We use the four initial values $\hat{\vartheta}^1(0) = (-0.5, 0.5)$, $\hat{\vartheta}^2(0) = (-2.5, 0)$, $\hat{\vartheta}^3(0) = (2.5, 2)$ and $\hat{\vartheta}^4(0) = (0, 2)$. We identify every solution $\hat{\vartheta}^i$ with its inverse mapping $\mathcal{O}_i^{-1}$ for $i \in \{1, \dots 4\}$. The angle θ is calculated directly from $\dot{T}$ and thus independent of the initial value. Consequently, only the angles ϑ are of interest and discussed in the following.

All four estimation errors can be found in Fig. 9. They admit different behaviour. The estimate $\hat{\vartheta}^1$ is the estimate considered in the previous section with its initial value in the basin of attraction of the real attitude. It converges to the real state until 150s. Then the estimation error increases and does not converge back to zero for the remainder of the simulation.

The other three estimates $\hat{\vartheta}^2$, $\hat{\vartheta}^3$, $\hat{\vartheta}^4$ all start at different initial values and follow different estimates. However, at 230 s they start following the real state ϑ. Note the discontinuity of all errors at 376 s. This is due to the bounded domain of ϑ to avoid ambiguities. The estimates are kept within a moving domain to avoid this discontinuity. However, they can easily be mapped into the real domain $[-\pi, \pi] \times [-\pi, \pi]$.

It can be seen that the estimates of the state is difficult to predict for the considered system if it crosses the set of unobservable states. At this point, the estimate which has been correct up to then can suddenly start to follow a wrong prediction as in the case of $\hat{\vartheta}_1$. Another possible result is that estimates which have been incorrect may start to converge to the correct solution as in the case of $\hat{\vartheta}_1$, $\hat{\vartheta}_2$, $\hat{\vartheta}_3$.

In order to evaluate whether all estimates really yield the same outputs and if it is possible to determine the correct estimate, the cost function is displayed in Fig. 10.

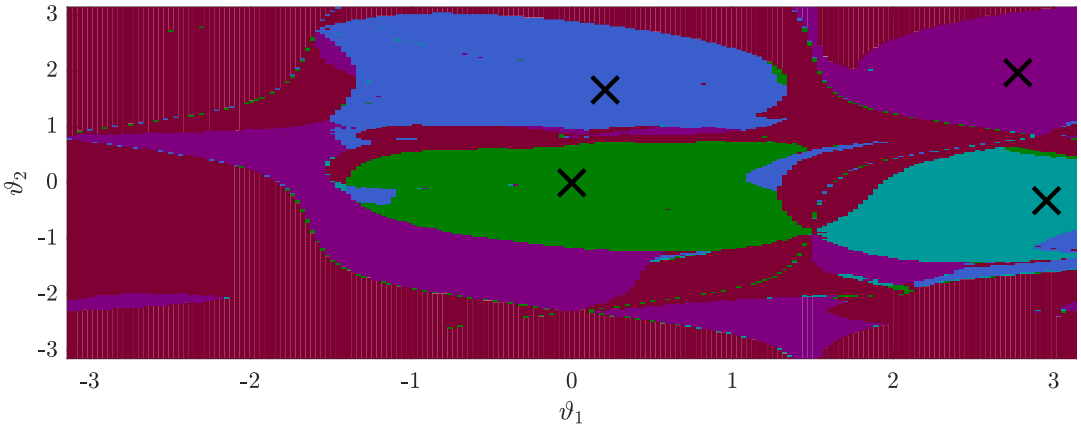

Fig. 6: Illustration of the basins of attraction of the four global minima. The global minima are marked by black crosses. The set of the initial values that do not converge to a global minimum are displayed in red. The basin of attraction of $\bar{\vartheta} = [0, 0]^\top$ which was used to construct the optimisation problem is displayed in green. The remaining colours correspond to the other three global minima.

TABLE I: Determined minima $\bar{\vartheta} \in \mathcal{LS}(\vartheta)$ and their rounded costs.

Minimum	$\begin{bmatrix}0\\0\end{bmatrix}$		$\begin{bmatrix}2.955\\-0.32\end{bmatrix}$	$\begin{bmatrix}2.77\\1.96\end{bmatrix}$	$\begin{bmatrix}0.208\\1.66\end{bmatrix}$	$\begin{bmatrix}-\pi\\-0.33\end{bmatrix}$	$\begin{bmatrix}-\pi\\2.2\end{bmatrix}$	$\begin{bmatrix}-2.23\\-\pi\end{bmatrix}$	$\begin{bmatrix}-\pi\\-\pi\end{bmatrix}$
Costs	2×10^{-8}		2×10^{-8}	2×10^{-8}	$2{\times}10^{-8}$	3×10^{-2}	0.1	5	8

TABLE II: Parameters and constants (all SI-units)

Parameter	Value	Parameter	Value
γ	0.0673	δ	1.6×10^{-11}
J	diag[5.4 5.4 0.9]	a_1	6.9×10^6
a_2	1.05×10^6	a_3	6.89×10^6
b_1	2.56	b_2	-1.64
b_3	-2.17	ω	0.001
$r_\oplus$	6371000	n	e_3

TABLE III: Initial states (all SI-units)

Parameter	Value
T	292
w	0.01[0.5774 0.5774 0.5774]
t	100
θ	$\frac{\pi}{2}$

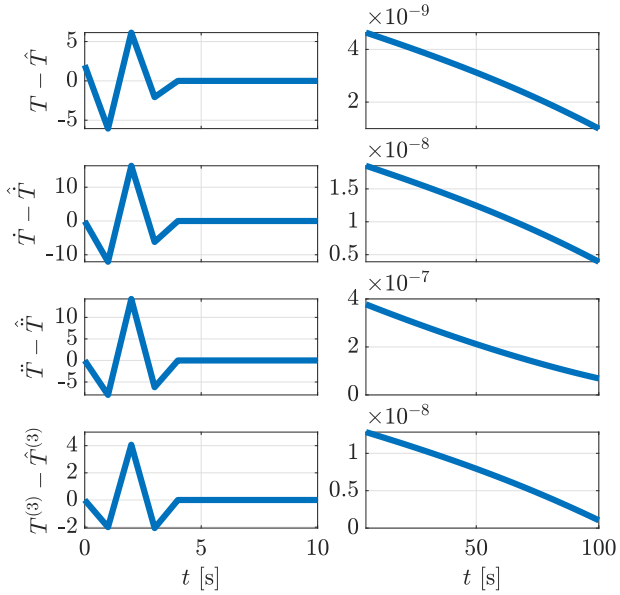

Fig. 7: Error between real and estimated temperature and their derivatives.

Based on the fact that $\hat{\vartheta}_1$ represents the correct estimate with only small numerical errors in the first 100 s, all costs below 10^{-7} suggest a good approximation. Thus, the complete $\hat{\vartheta}^1$, $\hat{\vartheta}^2$ trajectories can both be considered as attitude trajectories that lead to the same temperature. The estimates $\hat{\vartheta}^3$ and $\hat{\vartheta}^4$ between 94 s and 225 s have high costs. This suggests that during this phase the optimisation has not converged to a global minimum. This can be avoided by improving the optimisation using different methods or multiple initial values. In the remaining time, however, the estimated attitudes achieve the measured outputs as well.

These observations reveal an important issue. If the set of initial values contains points of multiple basins of attractions, it is not possible to distinguish the solutions by using the cost function. In the first 100 s there are four different attitude trajectories that lead to the same temperature and it cannot be determined which one is the desired one, solely inspecting the costs. Consequently, the initial states are either indistinguishable or the other three reconstructed trajectories are not a solution of the system (12) with $q = l_2^{r,n}(\theta, \vartheta_1, \vartheta_2)$. The latter can be verified by calculating the derivative of q using the difference quotient for $h = 1$ as well as the right hand side of (12)

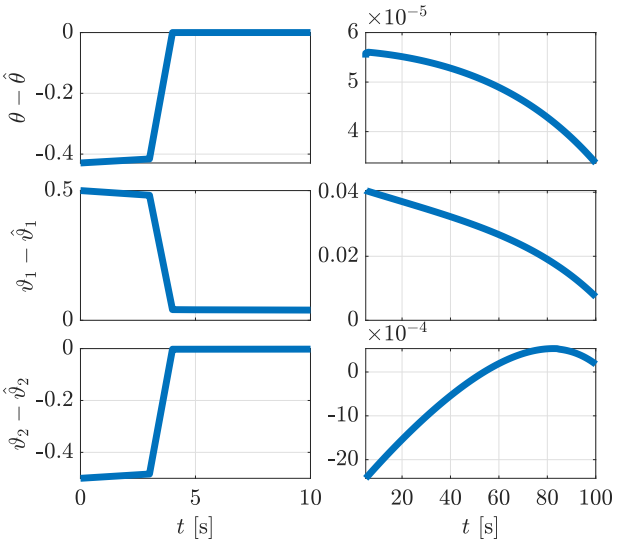

Fig. 8: Error between the real and estimated angles describing the attitude in radians.

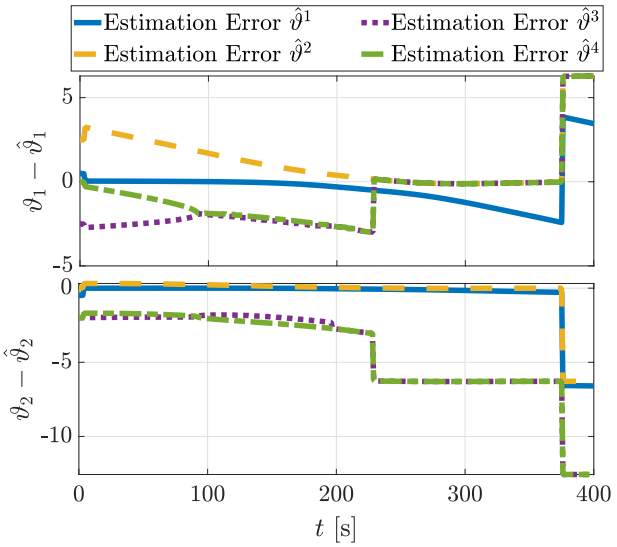

Fig. 9: Error angles for the four different initial states in radians.

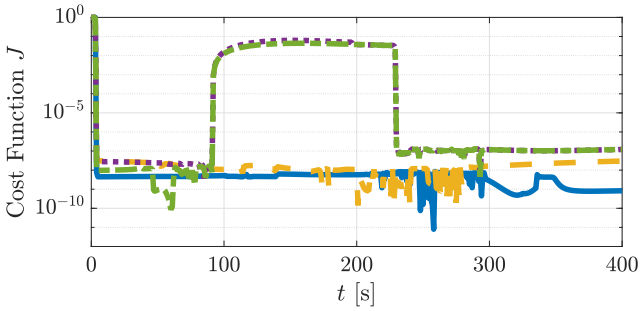

Fig. 10: Value of the cost function for the four estimates, line styles as in Figure 9.

and determine the difference between them

$$\varepsilon^q := \frac{q(t+h) - q(t)}{h} - \frac{1}{2}\Omega(\omega)q\,. \tag{32}$$

This variable is close to zero for a solution q which solves (12). It is displayed in Fig. 11 for the real and estimated states. It can be seen that for estimates close to the real attitude the error is relatively small. In the remaining time the error varies largely and is of high magnitude. In particular, the switch between the correct estimates around 225 s can be seen. This shows that despite the ambiguity, a real solution can be identified using information of a time interval of the estimation.

We use the final section of this work to illustrate the difficulties occurring under the influence of additional noise on the measurements and discuss natural augmentations to deal with them.

B. Measurements with Gaussian White Noise

Consider additional Gaussian white noise η_T, η_ω on the real temperature and angular velocity values, T and ω, respectively, i.e. the measured variables have the form $T_{\text{noisy}} = T + \eta_T$ and $\omega_{\text{noisy}} = \omega + \eta_\omega$. This leads to errors in the estimated temperature derivatives and optimal attitude solutions $(\hat{\theta}, \hat{\vartheta}_1, \hat{\vartheta}_2)$ that do not coincide with the real attitude. In turn, the provided initial value for the optimisation algorithm may lead to a diverging optimisation.

In order to reduce the influence of these potential errors, we adapt the algorithm illustrated in Figure 3. We filter the temperature measurements using a first order low pass filter $\dot{T}_{\text{fil}} = \frac{T_{\text{fil}}}{\tau} + \frac{T_{\text{noisy}}}{\tau_T}$ and smooth the angular velocity measurements using a simple observer $\omega_{\text{fil}} = f_\omega(\omega) + g_\omega u + w_{\text{noisy}} - \hat{w}$. Furthermore, in order to smooth the optimisation results and obtain an attitude that fulfils the dynamics (10), we process the attitude estimation obtained by the proposed algorithm with a nonlinear attitude filter in the spirit of [26] as

$$\dot{\hat{q}}_{\text{fil}} = \frac{1}{2}\Xi(\hat{q}_{\text{fil}})\omega + k\frac{1}{2}\Xi(\hat{q})\Xi^\top(\hat{q}_{\text{fil}})\hat{q}$$

where $\hat{q}$ is the attitude obtained by the optimisation and $\hat{q}_{\text{fil}}$ is the final estimated attitude and $(\hat{\theta}_{\text{fil}}, \hat{\vartheta}_{1,\text{fil}}, \hat{\vartheta}_{2,\text{fil}}) = l_1^{r,n}(\hat{q}_{\text{fil}})$ are the corresponding irradiation angles. The augmented algorithm is shown in Figure 12.

In the following, we show two simulations of the same scenario as before in Section VIII-A with the noise covariance parameters $\sigma_T = 10^{-4}\,\text{K}\,\text{s}^{-0.5}$, $\sigma_\omega = \sqrt{10}\cdot 10^{-7}\,\text{rad}\,\text{s}^{-0.5}$ and the estimated initial values $(\hat{\theta}^0, \hat{\vartheta}_1^0, \hat{\vartheta}_2^0)(t) = (\hat{\theta}, \hat{\vartheta}_1, \hat{\vartheta}_2)(t)$. The considered temperature noise is chosen smaller than the ones expected from real measurements [8]. This is done for illustration purposes as simulations with these noise levels already yield high errors in the estimation but allow an identification of the error sources. The two simulations differ by the given initial value for the optimisation. In the first scenario, the real attitude is given as the initial value $(\hat{\theta}^0, \hat{\vartheta}_1^0, \hat{\vartheta}_2^0)(t) = (\theta, \vartheta_1, \vartheta_2)(t)$

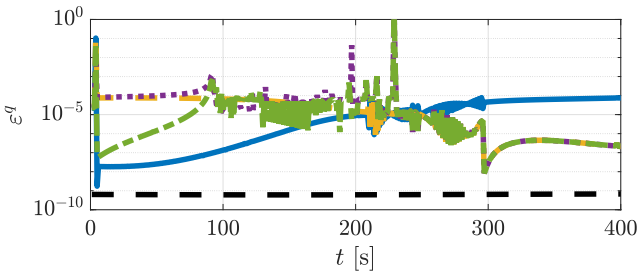

Fig. 11: Numerical quaternion derivative error as defined in (32) for the real quaternions (black dashed line) and the four estimates.

at the current time step t. This is a theoretical case as the real attitude is usually not available to the estimator. This first case is shown for illustration purposes to distinguish between errors induced by the deviations of the estimated derivatives and errors induced by a poor choice of the initial optimisation value. In the second simulation, the initial value of the optimisation is obtained from the filtered attitude of the last simulation step $(\hat{\theta}^0, \vartheta_1^0, \vartheta_2^0)(t) = (\theta_{\text{fil}}, \vartheta_{1,\text{fil}}, \vartheta_{2,\text{fil}})(t - T_s)$. The simulation step size is chosen to be $T_s = 0.1\,\text{s}$ while the optimisation is run at samples of 1 s to reduce the simulation time. The optimisation starts after 120 s to allow the convergence of the noise filter and the differentiator.

The gains in the simulations are $\alpha = \begin{bmatrix}8 & 24 & 32 & 16\end{bmatrix}$, $\varepsilon = 9.53$ and $\tau_T = 4.02$ which are obtained by an optimisation minimising the steady state error of the third estimated temperature derivative, i.e $\min_{\alpha,\varepsilon} \int_{150}^{400} |T^{(3)}(t) - \hat{T}^{(3)}(t)| \mathrm{d}t$. The observer gain $k = 0.02$ is determined by an optimisation minimising the error between the real and estimated attitude in the first simulation.

Figure 13 shows the error between the estimated and real temperature and their derivatives. The last two derivatives $\ddot{T}$ and $T^{(3)}$ are mainly responsible for the quality of the estimation of $\hat{\vartheta}_1$ and $\hat{\vartheta}_2$. It can be seen that the error is more than ten times higher as for the noise free case displayed in Figure 7. Additionally, the error does not converge to zero. This is significant as this error is propagated to the optimisation results as can be seen in Figure 14. This figure shows the errors between the real angles and the estimated angles. The errors to the estimated angles received from the optimisation $(\hat{\theta}, \hat{\vartheta}_1, \hat{\vartheta}_2)$ are displayed as light blue and orange dots, respectively. The errors to the filtered attitude $(\theta_{\text{fil}}, \vartheta_{1,\text{fil}}, \vartheta_{2,\text{fil}})$ are displayed as blue and red solid lines, respectively (c.f. also Figure 13). From the first figure it can be seen that the optimisation results $\hat{\theta}$ are identical for both simulations and very close to the real values. This is because the underlying optimisation problem (26a) for θ is simple to solve and requires only the first derivative of T. For the optimisation results of ϑ_1, ϑ_2 it can be seen that in the first simulation where the initial conditions are chosen to be the real values, the optimisation error mostly stays in a band of 1 rad around the real values. However, at some instances, e.g. between 237 s and 244 s, the optimisation does not give an estimation close to the real attitude even if it was given as an initial value. The reasons for that are twofold, first this divergence is close to the unobservable points discussed in Section VIII-A and secondly, the cost function changes considerably dependent on the magnitude of the error of the temperature derivative estimation. In the second simulation, it can be seen that the optimisation determines an estimation close to the global optimum $(2.77, 1.96)$ identified in the previous section which does not correspond to the real attitude but solves the optimisation problem. Consequently, the optimisation follows this optimum until around 227 s until the optimisation yields results closer to the real attitude.

For the filtered attitude it can be seen that the desired smoothing effect of the optimisation values is provided by the filter. However, an interesting result can be observed for both simulations. The errors that occur in the optimisation on the angles ϑ_1, ϑ_2 are propagated to errors of the filtered attitude in the θ angle. This can be observed for example by considering the optimisation results for the ideal initial values (dotted light blue) and the corresponding filtered attitude (solid blue). The optimisation has high $(\hat{\vartheta}_1, \hat{\vartheta}_2)$ errors between 200 s and 300 s. The filtered attitude however inherits these errors in θ_{fil} and not as expected in $(\hat{\vartheta}_{1,\text{fil}}, \hat{\vartheta}_{2,\text{fil}})$.

The simulations have shown that measurement noise is an important factor that needs to be dealt with when applying the proposed algorithm. We have proposed additional attitude and measurement filters that reduce the error induced by the measurement noise. Adaptations of the differentiator and the filters can be made to achieve potential improvements. We have investigated the usage of other linear differentiators such as Linear Kalman Filter. The considered linear differentiators admitted similar behaviour regarding their balance between performance and disturbance rejection properties. Thus, we expect improvements only through the usage of non-linear differentiators explicitely including the temperature derivative dynamics. Additionally, an attitude filter in $\theta, \vartheta_1, \vartheta_2$ instead of q may yield smaller errors in θ if the gains are chosen accordingly. In addition, the gains of the attitude filter may be made adaptive based on the costs obtained by the optimisation algorithm. For a high cost value the filter should rely more on the dynamics than on the correction term and therefore have a small gain k. The opposite reasoning can be made for a small cost function values.

IX. Conclusions

The attitude of a spacecraft can be estimated using only a single temperature measurement and angular velocity data. The governing system dynamics are highly nonlinear and transformed into canonical form using a standard observability mapping. A high gain observer is used to estimate the temperature and its derivatives. In order to determine the inverse of the observability mapping, a transformation of the attitude from quaternions to a set of three angles can be employed. The reduced order

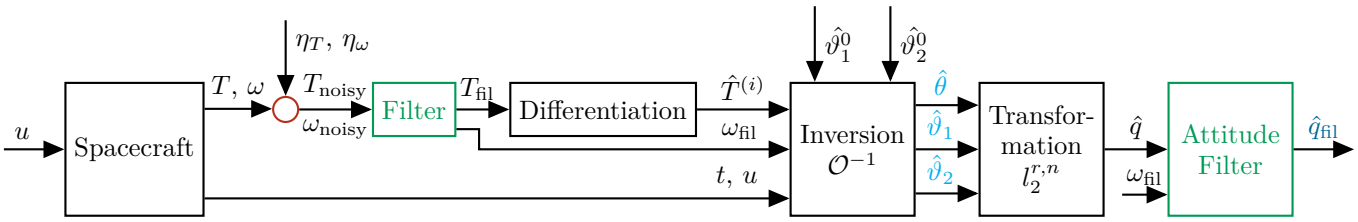

Fig. 12: Augmentation of the algorithm from Figure 3. The summation in red adds the considered measurement noise while the blocks in green are the additional filters. The attitude obtained from the optimisation $(\hat{\theta}, \hat{\vartheta}_1, \hat{\vartheta}_2)$ and after the filter $\hat{q}_{\text{fil}}$ are displayed in light blue and blue, respectively.

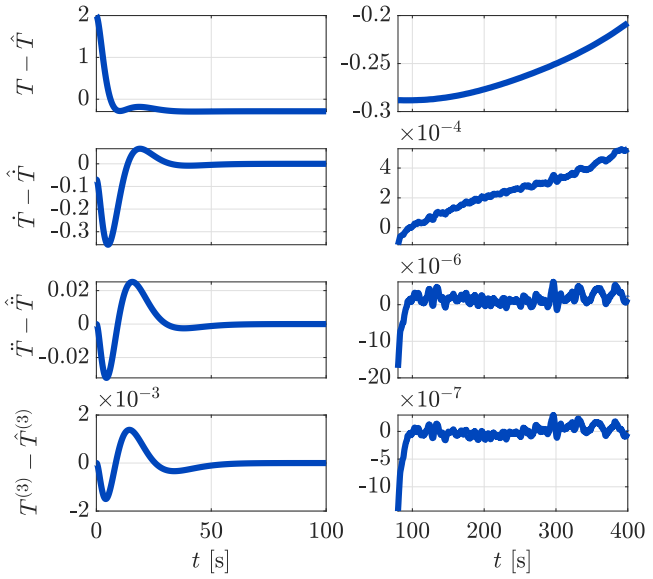

Fig. 13: Error between real and estimated temperature and their derivatives under the influence of measurement noise.

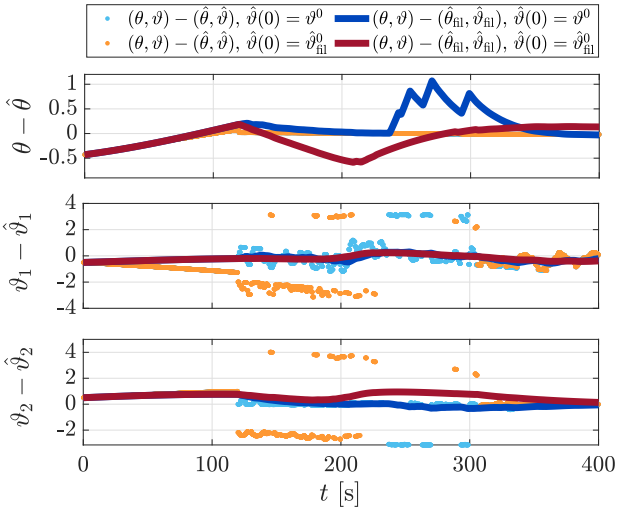

Fig. 14: Error between the estimated and real irradiation angles in radians.

inversion problem is then solved using optimisation. However, this observability mapping is not bijective and for the considered case four attitudes exist that produce the same temperature derivatives up to third order. The basins of attraction for the individual attitudes are calculated and illustrated. If it can be guaranteed that the initial value lies in the desired basin of attraction, the correct attitude can be estimated. If not, using multiple observers with different initial values is an option which allows to identify the correct estimate based on the error between the attitude dynamics. This is illustrated by means of numerical simulations. They show that even in this case the observer can estimate the attitude correctly for ideal measurements. The influence of noise on the temperature measurements leads to errors in the temperature derivative estimation and consequently to errors in the result of the optimisation. This is in particular an issue if the hereby generated initial value for the optimisation lies in an undesired domain of attraction. The remaining observable scenarios with albedo and solar irradiation will be investigated in future work. In this case, the proposed irradiation angle transformation does not lead to the desired order reduction which complicates the solution of the optimisation problem even more.

Appendix

A. Analytic Derivatives

This section contains the derivatives and Lie derivatives necessary for the transformation of the system into canonical form. For the partial derivatives of f_T at (T, q, t) with $r = r(t)$ and $\theta = \theta(q, t)$ we obtain

$$\frac{\partial f_T}{\partial T} = -4\delta T^3 \tag{33a}$$

$$\frac{\partial f_T}{\partial q} = \gamma \frac{\partial F(\theta(q,t), r(t))}{\partial \theta} \frac{\partial \theta(q,t)}{\partial q} \tag{33b}$$

$$\frac{\partial f_T}{\partial t} = \gamma \frac{\partial F(\theta(q,t), r(t))}{\partial \theta} \frac{\partial \theta(q,t)}{\partial t} + \gamma \frac{\partial F(\theta(q,t), r(t))}{\partial r} \dot{r} \tag{33c}$$

where $\dot{r}$ corresponds to the derivative of the position (9) with respect to time. With $H = \frac{\|r\|}{r_\oplus}$, the derivative of the

form factor for $r \neq 0$ is

$$\frac{\partial F(\theta,r)}{\partial \theta} = \begin{cases} -\frac{\sin(\theta)}{H^2} & \theta \leq \frac{\pi}{2} - \operatorname{asin}\left(\frac{1}{H}\right) \\ \frac{\partial F_2(\theta,r)}{\partial \theta} & \theta \in \Theta_2 \\ 0 & \theta > \frac{\pi}{2} + \operatorname{asin}\left(\frac{1}{H}\right) \\ \text{undefined} & \theta = \frac{\pi}{2} + \operatorname{asin}\left(\frac{1}{H}\right) \end{cases}$$

$$\frac{\partial F(\theta,r)}{\partial r} = \begin{cases} -2\frac{r_\oplus^2 r^\top}{\|r(t)\|^4}\cos(\theta) & \theta \leq \frac{\pi}{2} - \operatorname{asin}\left(\frac{1}{H}\right) \\ \frac{\partial F_2(\theta,r)}{\partial r} & \theta \in \Theta_2 \\ 0 & \theta > \frac{\pi}{2} + \operatorname{asin}\left(\frac{1}{H}\right) \\ \text{undefined} & \theta = \frac{\pi}{2} + \operatorname{asin}\left(\frac{1}{H}\right) \end{cases}$$

with $\Theta_2 = \{\theta \mid \frac{\pi}{2} - \operatorname{asin}\left(\frac{1}{H}\right) < \theta < \frac{\pi}{2} + \operatorname{asin}\left(\frac{1}{H}\right)\}$ where $\frac{\partial F_2(\theta,r)}{\partial \theta}$ is calculated symbolically using computer algebra. The partial derivatives of the angle θ are

$$\begin{aligned} \frac{\partial \theta(q,t)}{\partial t} &= \frac{\mathrm{d}\operatorname{acos}(-\frac{r^\top}{\|r\|}A(q)^\top n)}{\mathrm{d}x}\frac{\partial \cos(\theta)}{\partial t} \\ \frac{\partial \cos(\theta)}{\partial t} &= -n^\top A(q)\frac{\partial}{\partial r}\left(\frac{r}{\|r\|}\right)\dot{r} \\ \frac{\partial}{\partial r}\left(\frac{r}{\|r\|}\right) &= \frac{1}{\|r\|^3}\begin{bmatrix} r_2^2+r_3^2 & -r_1r_2 & -r_1r_3 \\ -r_1r_2 & r_1^2+r_3^2 & -r_2r_3 \\ -r_1r_3 & -r_2r_3 & r_1^2+r_2^2 \end{bmatrix} \\ \frac{\partial \theta(q,t)}{\partial q} &= \frac{\mathrm{d}\operatorname{acos}(-\frac{r^\top}{\|r\|}A(q)n)^\top}{\mathrm{d}x}\frac{-r^\top}{\|r\|}\frac{\partial A(q)^\top n}{\partial q} \end{aligned}$$

and the derivative of the rotation matrix is given in [2] as

$$\frac{\partial A(q)n}{\partial q} = 2\|q\|^{-2}[A(q)n\times]\Xi^\top(q) \tag{34}$$

and thus

$$\frac{\partial A(q)^\top n}{\partial q} = 2\|q\|^{-2}[A(I_{\mathrm{mp}}q)n\times]\Xi^\top(I_{\mathrm{mp}}q)I_{\mathrm{mp}}$$

where $I_{\mathrm{mp}} = \begin{pmatrix} -I_3 & 0 \\ 0 & 1 \end{pmatrix}$ and $A(q)^\top = A(I_{\mathrm{mp}}q)$. It is readily verified that

$$\frac{\partial}{\partial T}\frac{\partial f_T(T,q,t)}{\partial q} = 0 \tag{35}$$

$$\frac{\partial}{\partial T}\frac{\partial f_T(T,q,t)}{\partial t} = 0 \tag{36}$$

$$\frac{\partial}{\partial q}\left(\frac{\partial f_T(T,q)}{\partial T}f_q(q,\omega)\right) = \frac{\partial f_T(T,q)}{\partial T}\frac{\partial f_q(q,\omega)}{\partial q}\,. \tag{37}$$

We use this to obtain the Lie derivatives

$$h(x) = T \tag{38a}$$

$$\mathcal{L}_f h(x) = f_T(T,q,t) \tag{38b}$$

$$\begin{aligned} \mathcal{L}_f^2 h(x) = {} & \frac{\partial f_T(T,q,t)}{\partial T}f_T(T,q,t) \\ & + \frac{\partial f_T(T,q,t)}{\partial q}f_q(q,\omega) + \frac{\partial f_T(T,q,t)}{\partial t} \end{aligned} \tag{38c}$$

$$\begin{aligned} \mathcal{L}_f^3 h(x) = {} & \frac{\partial}{\partial T}\left(\frac{\partial f_T(T,q,t)}{\partial T}f_T(T,q,t)\right)f_T(T,q,t) \\ & + \left(\frac{\partial f_T(T,q,t)}{\partial T}\frac{\partial f_T(T,q,t)}{\partial q}\right. \\ & \quad + f_q(q,\omega)^\top\frac{\partial^2 f_T(T,q,t)}{\partial q^2} \\ & \quad + \frac{\partial f_T(T,q,t)}{\partial q}\frac{\partial f_q(q,\omega)}{\partial q} \\ & \quad \left. + \frac{\partial}{\partial q}\frac{\partial f_T(T,q,t)}{\partial t}\right)f_q(q,\omega) \\ & + \frac{\partial f_T(T,q,t)}{\partial q}\frac{\partial f_q(q,\omega)}{\partial \omega}f_\omega(\omega) \\ & + \frac{\partial f_T(T,q,t)}{\partial T}\frac{f_T(T,q,t)}{\partial t} \\ & + \frac{\partial}{\partial t}\frac{\partial f_T(T,q,t)}{\partial q}f_q(q,\omega) + \frac{\partial^2 f_T(T,q,t)}{\partial t^2} \end{aligned} \tag{38d}$$

$$\mathcal{L}_g\mathcal{L}_f^2 h(x) = \frac{\partial f_T(T,q,t)}{\partial q}\frac{\partial f_q(q,\omega)}{\partial \omega}g_\omega\,. \tag{38e}$$

References

[1] M. J. Sidi, *Spacecraft Dynamics and Control: a Practical Engineering Approach*, vol. 7. Cambridge University Press, 1997.

[2] F. L. Markley and J. L. Crassidis, *Fundamentals of Spacecraft Attitude Determination and Control*. Springer, 2014.

[3] J. L. Crassidis and F. L. Markley, "Unscented filtering for spacecraft attitude estimation," *Journal of Guidance, Control, and Dynamics*, vol. 26, no. 4, pp. 536–542, 2003.

[4] A. Labibian, S. Pourtakdoust, A. Alikhani, and H. Fourati, "Development of a radiation based heat model for satellite attitude determination," *Aerospace Science and Technology*, vol. 82, pp. 479–486, 2018.

[5] A. Labibian, S. H. Pourtakdoust, M. Kiani, A. A. Sheikhi, and A. Alikhani, "Experimental validation of a novel radiation based model for spacecraft attitude estimation," *Sensors and Actuators A: Physical*, vol. 250, pp. 114–122, 2016.

[6] F. N. Gourabi, M. Kiani, and S. H. Pourtakdoust, "Autonomous temperature-based orbit estimation," *Aerospace Science and Technology*, vol. 86, pp. 671–682, 2019.

[7] F. N. Gourabi, M. Kiani, and S. H. Pourtakdoust, "On-line orbit and albedo estimation using a strong tracking algorithm via satellite surface temperature data," *IEEE Transactions on Aerospace and Electronic Systems*, 2020.

[8] H. B. Khaniki and S. H. Karimian, "Satellite attitude determination using absorbed heat fluxes," *Journal of Aerospace Engineering*, vol. 29, no. 6, p. 04016053, 2016.

[9] A. Labibian, A. Alikhani, and S. H. Pourtakdoust, "Performance of a novel heat based model for spacecraft attitude estimation," *Aerospace Science and Technology*, vol. 70, pp. 317–327, 2017.

[10] H. J. Kramer, *Observation of the Earth and its Environment: Survey of Missions and Sensors*. Springer, 2002.

[11] J. Levenhagen, N. Duske, and R. Wolters, "Earth oriented safe mode design based on the EADS astrium CESS," *IFAC Proceedings Volumes*, vol. 40, no. 7, pp. 301–304, 2007.

[12] T. Posielek and J. Reger, "Observability analysis for spacecraft attitude determination using a single temperature sensor," in *European Control Conference*, pp. 1432–1439, 2021.
[13] T. Posielek and J. Reger, "A novel attitude representation in view of spacecraft attitude reconstruction using temperature data," in *Conference on Modelling, Identification and Control of Nonlinear Systems*, pp. 526–531, 2021.
[14] T. Posielek, "A Modelica library for spacecraft thermal analysis," in *Proceedings of The American Modelica Conference*, no. 154, pp. 46–55, Linköping University Electronic Press, 2019.
[15] W. J. Larson and J. R. Wertz, *Space Mission Analysis and Design*. Springer, 1991.
[16] J. Meseguer, I. Pérez-Grande, and A. Sanz-Andrés, *Spacecraft Thermal Control*. Woodhead Publishing, 2012.
[17] G. Wahba, "A least squares estimate of satellite attitude," *SIAM Review*, vol. 7, no. 3, p. 409, 1965.
[18] G. Besançon, *Nonlinear Observers and Applications*, vol. 363. Springer, 2007.
[19] Texas Instruments, *TMP117 High-Accuracy, Low-Power, Digital Temperature Sensor*, 2021.
[20] Maxim Integrated, *MAX30208, Low-Power, High-Accuracy Digital Temperature Sensor*, 2020.
[21] H. K. Khalil and J. W. Grizzle, *Nonlinear Systems*, vol. 3. Prentice hall Upper Saddle River, NJ, 2002.
[22] A. Levant, "Robust exact differentiation via sliding mode technique," *Automatica*, vol. 34, no. 3, pp. 379–384, 1998.
[23] B. Addis, M. Locatelli, and F. Schoen, "Local optima smoothing for global optimization," *Optimization Methods and Software*, vol. 20, no. 4-5, pp. 417–437, 2005.
[24] H.-D. Joos, J. Bals, G. Looye, K. Schnepper, and A. Varga, "A multiobjective optimisation-based software environment for control systems design," in *IEEE International Conference on Control Applications and International Symposium on Computer Aided Control Systems Design*, pp. 7–14, 2002.
[25] D. Henrion, J.-B. Lasserre, and J. Löfberg, "Gloptipoly 3: moments, optimization and semidefinite programming," *Optimization Methods & Software*, vol. 24, no. 4-5, pp. 761–779, 2009.
[26] A. Tayebi, "Unit quaternion observer based attitude stabilization of a rigid spacecraft without velocity measurement," in *IEEE Conference on Decision and Control*, pp. 1557–1561, IEEE, 2006.

Tobias Posielek received his bachelor's and master's degree in Engineering Cybernetics and Systems Theory from the TU Ilmenau, Germany in 2015 and 2017, respectively. Currently, he is with the Institute of System Dynamics and Control of the German Aerospace Center Oberpfaffenhofen (DLR-SR) and pursuing his doctoral degree in Systems and Control Engineering. His current research interests include nonlinear systems, observer design, spacecraft attitude control and sliding mode control.

Johann Reger received his diploma degree (Dipl.-Ing.) in Mechanical Engineering in 1999 and his doctorate (Dr.-Ing.) in Control Engineering in 2004, both from the University of Erlangen-Nuremberg in Germany. He has held several postdoc positions, among others, with the Mechatronics Department at CINVESTAV-IPN in Mexico-City, the EECS Control Laboratory at the University of Michigan in Ann Arbor, and the Control Systems Group at TU Berlin. Since 2008 he is a full professor and head of the Control Engineering Group at the Computer Science and Automation Faculty, TU Ilmenau, in Germany. There he also serves as vice-dean and director of the Institute for Automation and Systems Engineering. His current research foci are on adaptive and robust control, variable structure and sliding mode control, state and parameter estimation. Application areas include robotics, mechatronics, automotive, and water systems.